Supporting Information:

Lewis Acidic Boron-Oxygen Interactions Activate Cobalt Oxysulfide for Oxygen Evolution Reaction

*Abhirami V. Krishnan[‡a], Aruna Narayanan Nair[‡a], Charles Matlock[b], Kavish Saini[a], Sisheed Sivaraman[a], Deepesh Gopalakrishnan[a], Ning Zhang[b], and Sreeprasad T. Sreenivasan[*a]*

[a]Department of Chemistry and Biochemistry, The University of Texas at El Paso, El Paso, TX, 79968, United States

[b]Mechanical Engineering, Baylor University, Waco, TX, 76706, United States

[‡] These authors contributed equally to this work.

***Corresponding Author** *:* Sreeprasad T. Sreenivasan; Email: sreenivasan@utep.edu, Phone number; +1 (915) 747-6833, *https://orcid.org/0000-0002-5728-0512*

Chemicals

All reagents and solvents were commercially available and used without further purification. Cobalt nitrate hexahydrate [$Co(NO_3)_2.6H_2O$], Thioacetamide [CH_3CSNH_2], Polyvinylpyrrolidone [$(C_6H_9NO)_n$], Sodium borohydride [$NaBH_4$]**,** Ethanol, Potassium hydroxide were purchased from Sigma–Aldrich . Nafion binder (5 wt.%) was purchased from Ion power.

Synthesis

In a typical synthesis of CoO_xS_y, 0.291 g (1 mmol) of $Co(NO_3)_2 \cdot 6H_2O$ powder was dissolved in 50 mL of deionized water and then 0.15 g (2 mmol) of thioacetamide and 0.07g of PVP was added into above solution and stirred at room temperature for 1h. Subsequently, the solution was transferred into a 50 mL of Teflon-lined stainless-steel autoclave and heated at 120°C for 24 h. After cooling naturally, the resultant black powder was collected and washed several times by deionized water and ethanol. Further the sample was dried in a hot air oven at 60 °C for 4h and used for further characterizations. The Boron doped CoO_xS_y sample was synthesized in a similar procedure, the corresponding dopant precursor $NaBH_4$ (3.78 mg, 0.1 mmol) was added to the solution prior to hydrothermal process.

Characterization

Structural characterization of the CoO_xS_y and Boron doped CoO_xS_y performed using Powder X-ray Diffraction (PXRD) was performed via Empyrean 2 PANanalytical diffractometer with a Cu Kα (λ = 1.5418 Å) radiation source. The morphology of the CoO_xS_y and Boron doped CoO_xS_y was examined using a nanoSEM 450 from FEI company scanning electron microscope equipped with an oxford EDAX energy-dispersive X-ray spectroscopy (EDS) system. SEM-EDS measurements were performed at an accelerating voltage of 10-15kV at spot size 2.5, with a typical data acquisition time of seconds (dwell time 10-20us). Transmission electron microscopy (TEM) analysis of the CoO_xS_y and Boron doped CoO_xS_y was performed using instrument Tecnai G2 F30-S TWIN microscope at 300kV with Gatan Ultrascan 2k × 2k CCD, 4-30 fps detector. The samples were prepared by dry deposition of the powder onto an ultrathin carbon-coated copper grid (Ted Pella Inc.). Raman scattering spectra were measured using the high-resolution NT MDT Spectra II spectrometer (100x objective) equipped with a green laser (532 nm) using 600 lines/mm gratings. The laser power was ~10mW/μm^2 .

Electrochemical measurements

The electrocatalytic performance of all catalysts was analyzed using a CHI6372E CH instrument workstation. All the experiments were performed in a three-electrode configuration using platinum wire as a counter electrode, Hg/HgO as a reference electrode, and a glassy carbon electrode (3 mm diameter) as a working electrode. The electrolyte used was a 1 M aqueous KOH solution. The OER activity was obtained via LSV at a low scan rate of 5 mV s^{-1}. For the preparation of the working electrode, a finely powdered catalyst (5 mg) and 20 μL of a Nafion (5 wt %) solution were dispersed in isopropanol (1 mL). The solution was ultrasonicated for 30 min to acquire an ink type suspension. Ten microliters of this ink were drop-casted on the surface of the glassy carbon electrode and dried in an oven at 30 °C and used as the working electrode.

Tafel slopes: The Tafel slope was determined by fitting the overpotential (η) against the logarithm of the current density (log j) using the Tafel equation,

$$\eta = b \times \log\left(\frac{j}{j_0}\right) \quad \ldots\ldots(S2)$$

under the assumption that the concentrations in the bulk and at the electrode–electrolyte interface are identical. In this equation, *b* represents the Tafel slope, *j* is the current density, and j_0 denotes the exchange current density.

Electrochemical Impedance Spectroscopy: EIS measurements were done on the frequency ranges from 10^5 to 10^{-1} Hz .

Electrochemical Double Layer Capacitance (C_{dl}): Cyclic voltammetry (CV) measurements were conducted at different scan rates within a potential window where no Faradaic processes occur (V vs Hg/HgO) to estimate the electrochemical double-layer capacitance associated with OER. Difference between cathodic and anodic current densities (ΔJ) was plotted against varying scan rates for all the catalysts. The slope of this ΔJ versus scan rate plot gives the electrochemical double-layer capacitance (C_{dl}) value.

Electrochemical Active Surface Area (ECSA): The ECSA was measured by determining the electrochemical double layer capacitance (C_{dl}) using the following equations,

$$ECSA = {C_{dl}}/{C_s} \quad \ldots\ldots(S3)$$

"Cs" denotes a specific capacitance value of 0.040 mF cm^{-2} depending on the typical reported values.[1, 2] evaluate the specific activity of the catalysts, the geometrically normalized current density was further normalized by the electrochemical active surface area (ECSA), as

$$J_{ECSA} = {J_{geo}}/{ECSA^{geo}} \quad \text{.....(S4)}$$

Density Functional Theory Calculations

Density functional theory (DFT) calculations were performed using the Vienna *ab initio* Simulation Package (VASP) employing the projector augmented wave (PAW) method within the Perdew–Burke–Ernzerhof (PBE) generalized gradient approximation.[3, 4] Amorphous Co–S–O and B-doped Co–S–O models were constructed from a 2 × 2 × 2 CoS_2 supercell (80 atoms), where structural disorder was introduced via vacancy generation followed by full ionic relaxation to approximate the experimentally observed amorphous framework. The bottom layer of atoms in the model was fixed at the ground-state lattice parameters, while the top layers were allowed to move freely, a technique used in previous work .[5-7] The results from XRD indicate an amorphous structure; however, accurate amorphous structures are challenging to model using periodic boundary conditions[6, 8, 9]. The amorphous structure was created by removing eight atoms inside the model, creating vacancies that cause the structure to become amorphous following an ionic relaxation.[6] A 20 Å vacuum layer was applied along the surface-normal direction to eliminate spurious periodic interactions. Initial low-precision relaxations were conducted using a 400 eV plane-wave cutoff and a 3 × 3 × 1 k-point mesh, followed by high-precision relaxations with a 520 eV cutoff and stricter convergence criteria (energy < 10^{-6} eV, force < 0.02 eV $Å^{-1}$). Static calculations employing an 8 × 8 × 1 Γ-centered k-mesh and the tetrahedron method with Blöchl corrections were performed to obtain projected density of states (PDOS). Bader charge analysis was conducted to quantify charge redistribution upon oxygen and boron incorporation. Hydroxide adsorption energies were calculated by placing OH species on surface Co, S, O, and B sites, followed by full structural relaxation, enabling evaluation of site-dependent binding energetics relevant to the OER process.

The DFT model compositions were chosen as representative relaxed amorphous local-composition models rather than exact stoichiometric phase assignments for the experimental catalyst. Because finite-cell amorphous modeling permits only discrete accessible compositions, exact reproduction of the experimental composition is not possible within a tractable supercell. The selection of oxygen-containing and boron-incorporated models was guided by both energetic screening (Tables S3 and S4) and the experimental XPS trends. In particular, comparison of the XPS survey compositions of CoO_xS_y and B-CoO_xS_y shows that,

after normalizing Co to 1, the O/Co ratio decreases from 6.3 to 1.9, whereas the S/Co ratio changes only modestly from ~2.5 to ~2.1. Together with the B 1s features assignable to B-O/B-M environments, this suggests that boron incorporation most strongly perturbs the oxygen-containing local environments of the amorphous Co-O-S host. Therefore, the DFT analysis was constructed by first identifying stable oxygen-containing Co-S models and then introducing boron into these oxygenated frameworks to probe its effect on charge redistribution and $^{-}$OH adsorption.

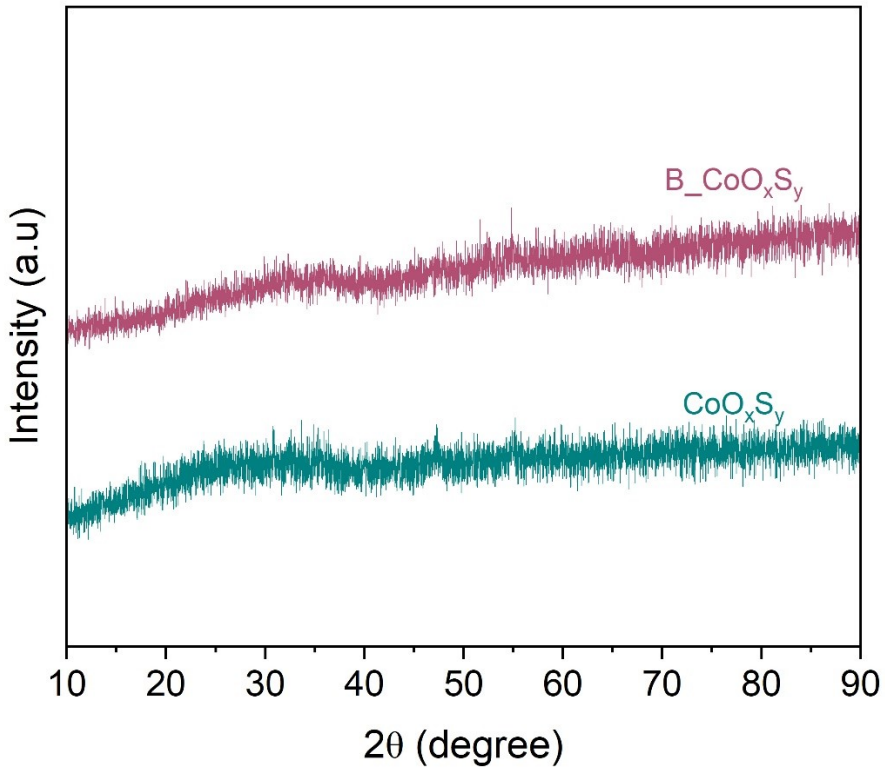

Figure S1. Powder X-ray diffraction (PXRD) patterns of CoO_xS_y and B-CoO_xS_y

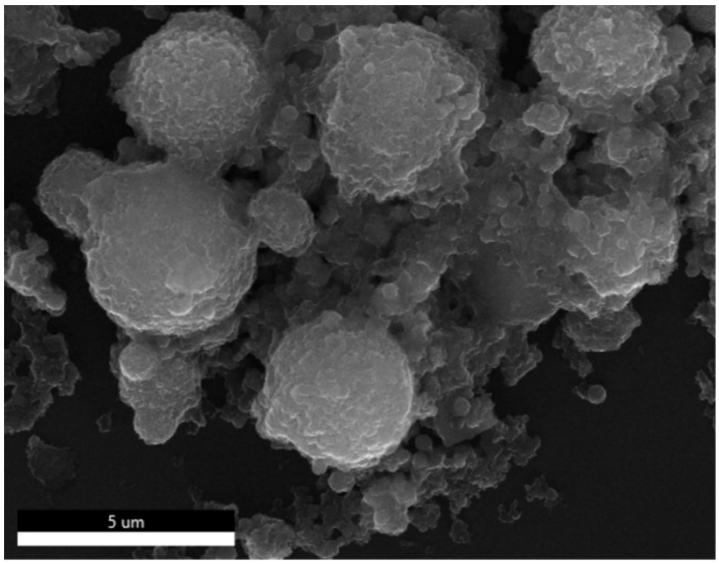

Figure S2. Scanning Electron Microscopy (SEM) image of CoO_xS_y

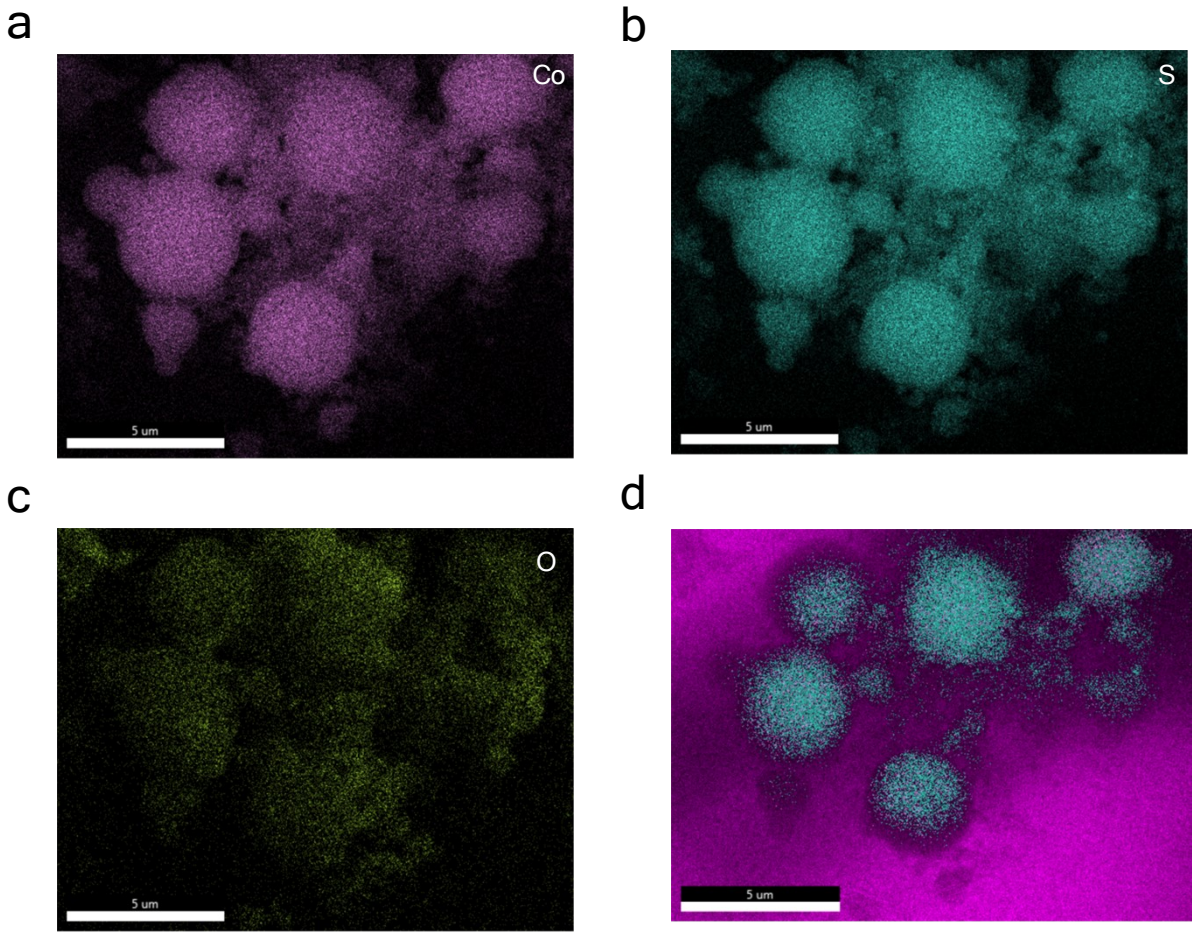

Figure S3. Elemental mapping image of CoO_xS_y

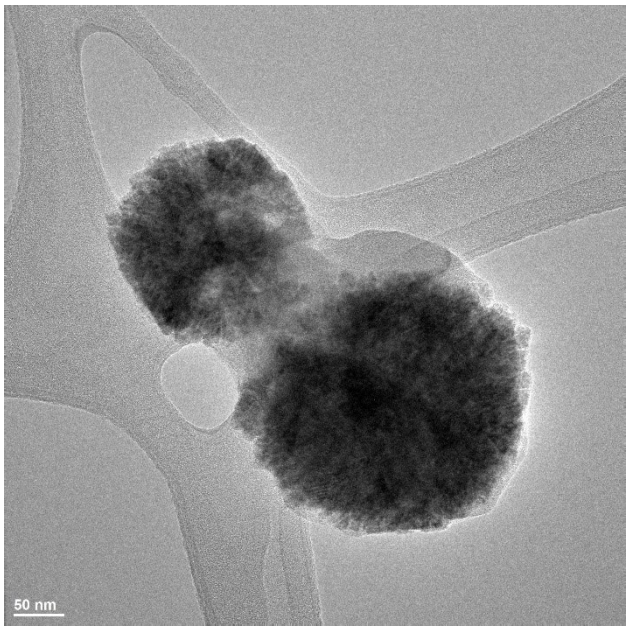

Figure S4. High Resolution Transmission Electron Microscopy (HR-TEM) image of CoO_xS_y

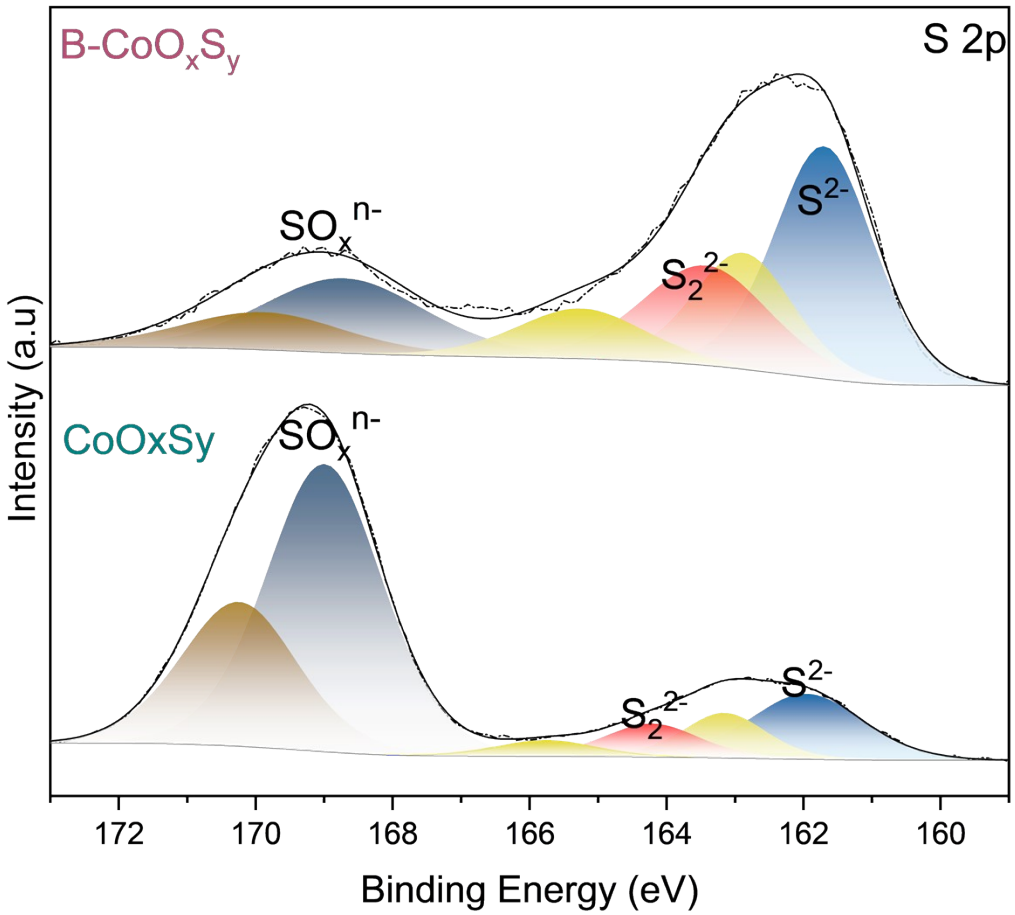

Figure S5. S2p X-ray photoelectron Spectroscopy (XPS) spectra of CoO_xS_y and B-CoO_xS_y

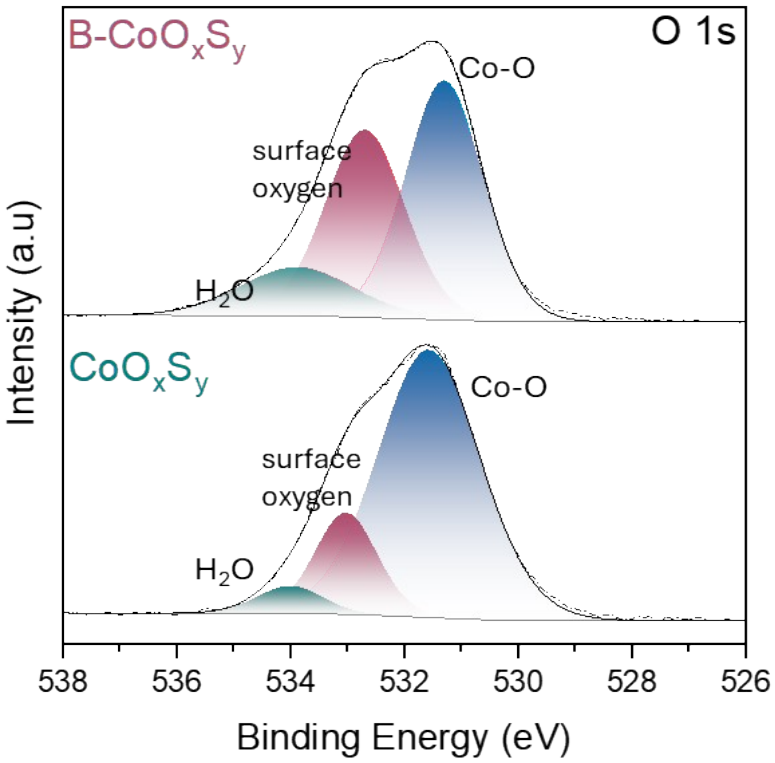

Figure S6. O1s X-ray photoelectron Spectroscopy (XPS) spectra of CoO_xS_y and B-CoO_xS_y

The O 1s region was deconvoluted into a dominant Co-O related oxygen component, together with higher-binding-energy contributions from surface oxygen species, including hydroxyls, and adsorbed H_2O.

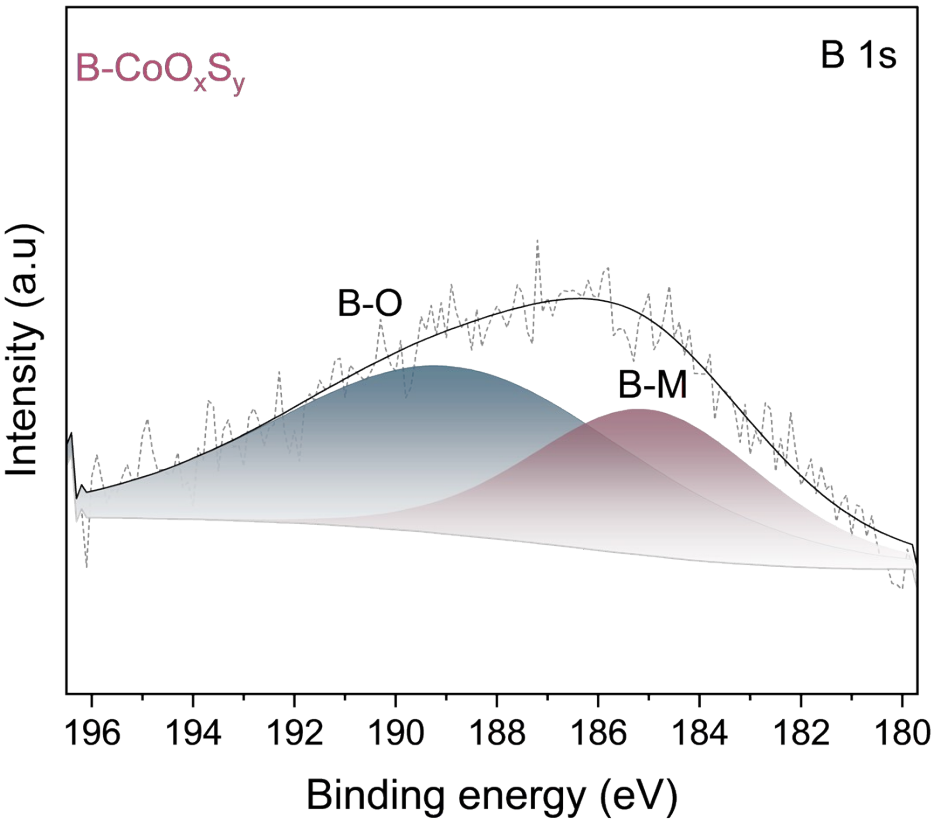

Figure S7. B1s XPS spectra of B-CoO$_x$S$_y$

Table S1. XPS peak positions and binding energy shifts for CoO_xS_y and B-CoO_xS_y

Region	Peak Assignment	CoO_xS_y (eV)	B-CoO_xS_y (eV)	Shift (ΔBE, eV)
Co $2p_{3/2}$	Co^{3+}	~778.51	~778.24	**-0.27**
S $2p_{3/2}$	Metal-S	~161.95	~161.69	**-0.26**
O 1s	Co-O	~531.57	~531.29	**-0.28**
O 1s	Surface oxygen	~533.02	~532.69	**-0.33**

Table S2. XPS-derived atomic percentages of CoO_xS_y and B doped CoO_xS_y .

Element	Core Level	Before Doping	After Doping
Cobalt	Co 2p	10.19	17.8
Oxygen	O 1s	64.25	33.75
Sulfur	S 2p	25.56	36.53
Boron	B 1s	NA	11.92

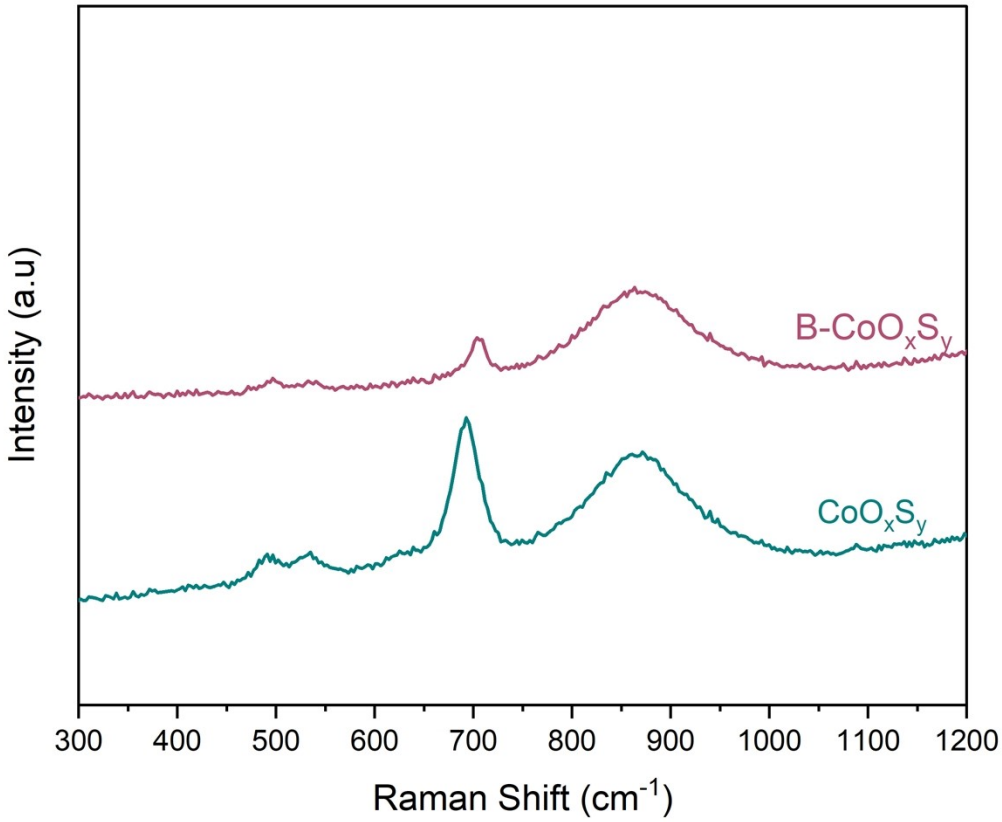

Figure S8. Raman spectra of the CoO_xS_y and B-CoO_xS_y.

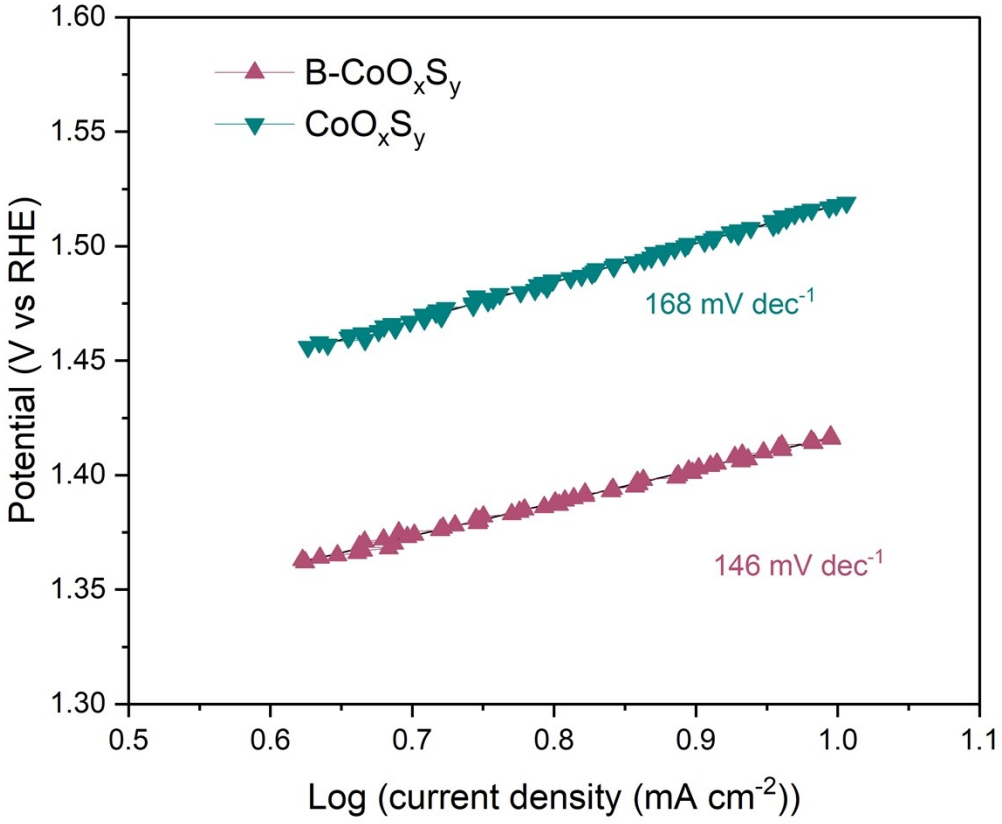

Figure S9. Tafel slopes derived from the polarization data of CoO_xS_y and B-CoO_xS_y.

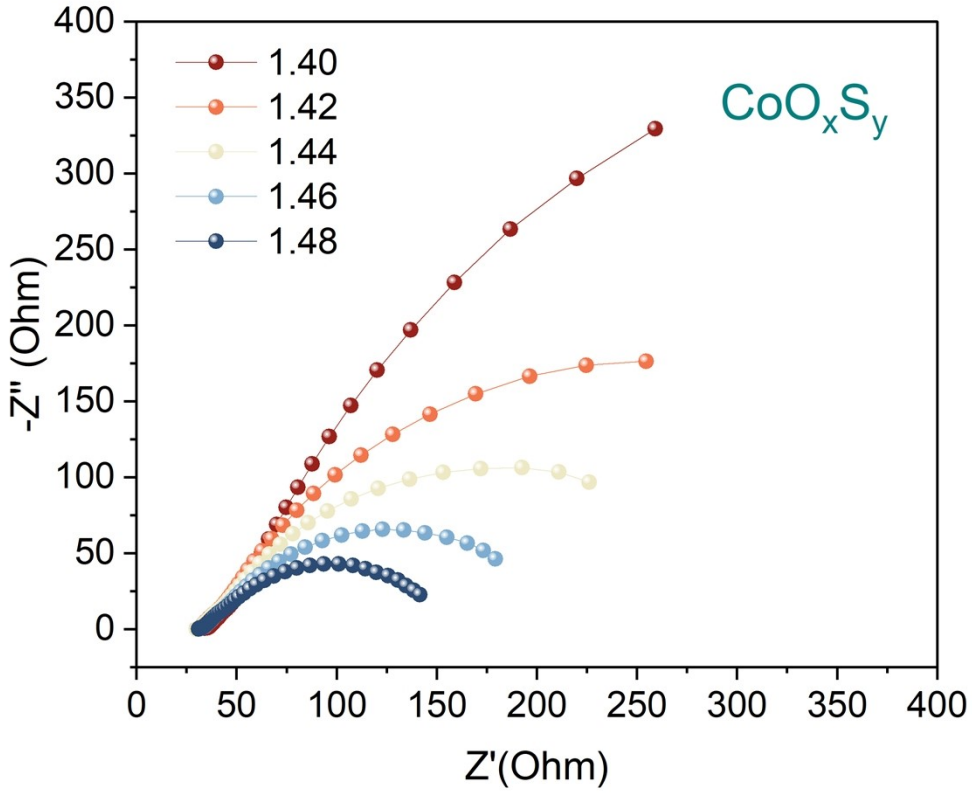

Figure S10. Electrochemical Impedance Spectroscopy (EIS) measurement for CoO_xS_y

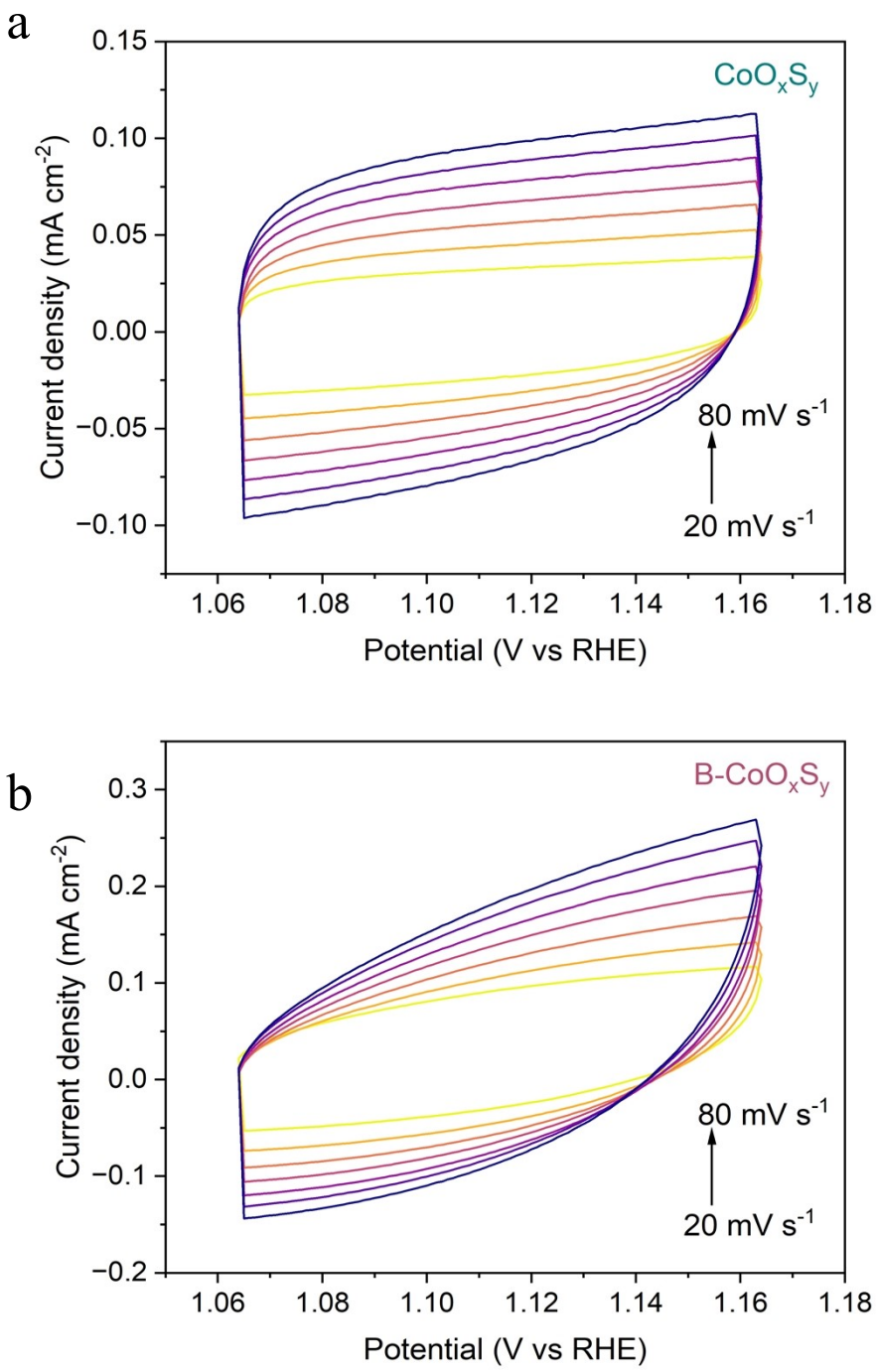

Figure S11. (a-b) Cyclic voltammograms (CV) of CoO_xS_y and B-CoO_xS_y recorded in the non-faradaic region at scan rates from 20 mV s^{-1} to 80 mV s^{-1} respectively.

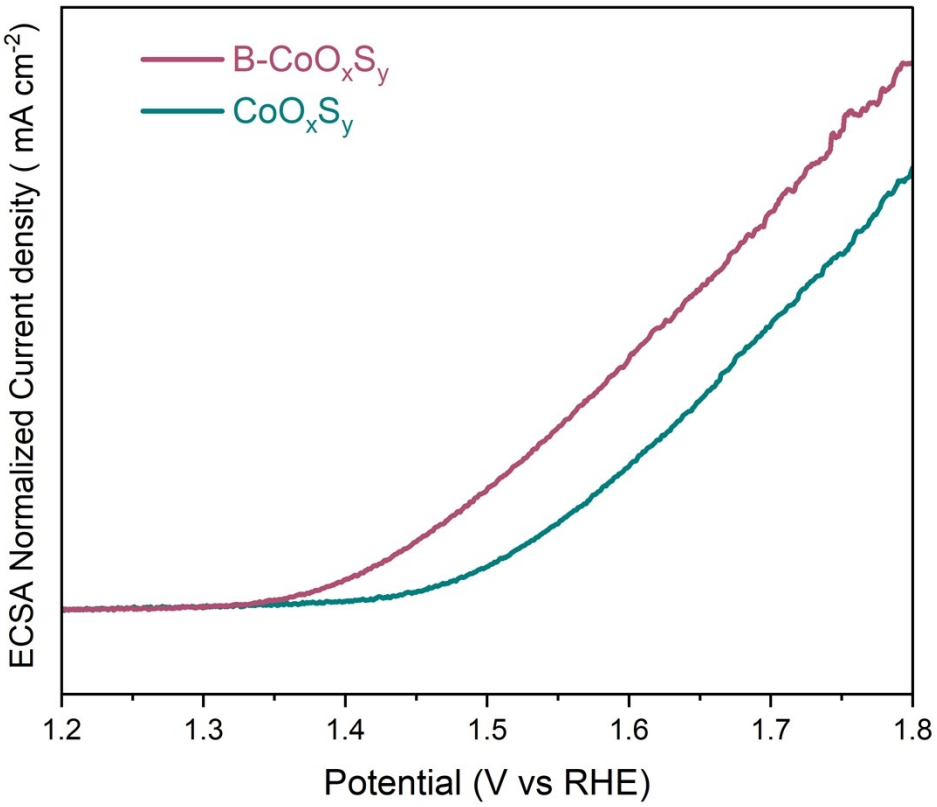

Figure S12. ECSA normalized polarization curves of CoO_xS_y and B-CoO_xS_y

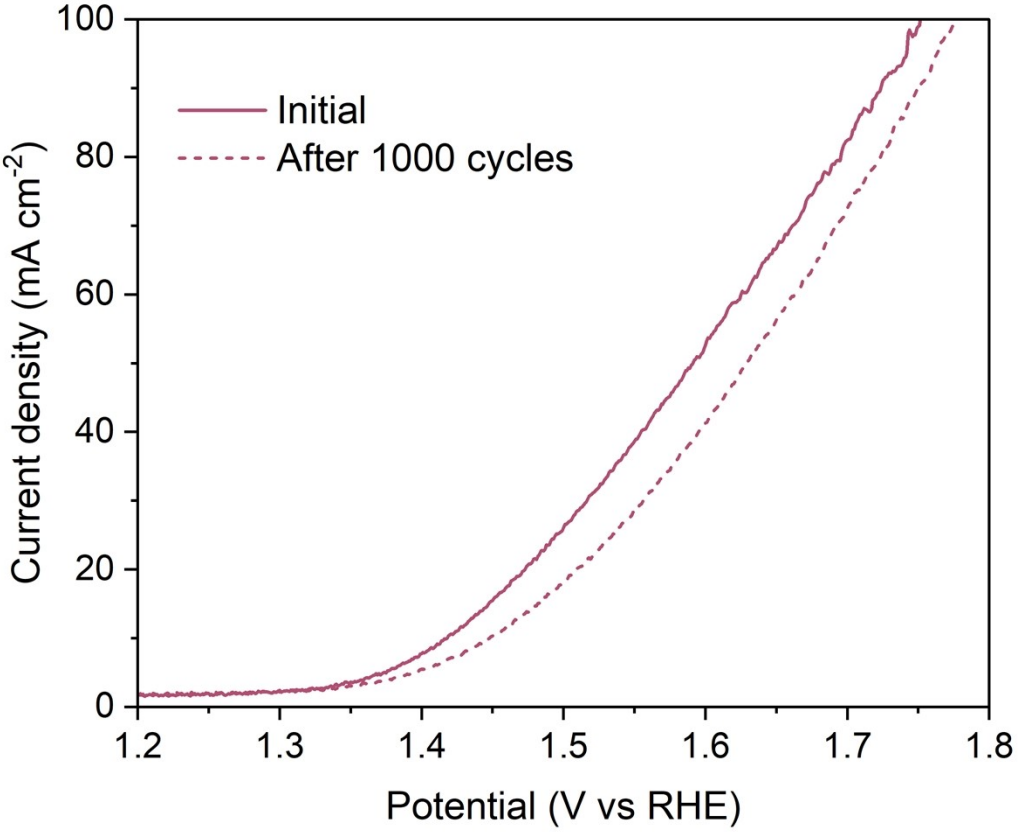

Figure S13. Polarization curves before and after durability test of B-CoO_xS_y

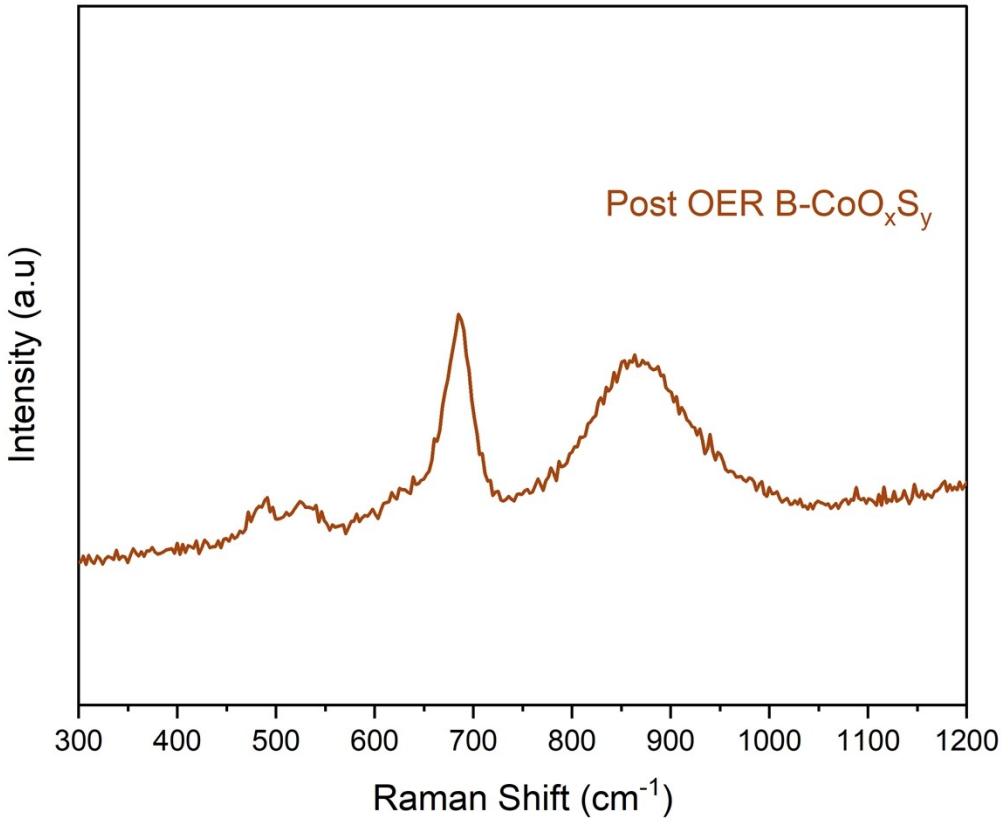

Figure S14. Raman spectrum of the B-CoO_xS_y post OER studies.

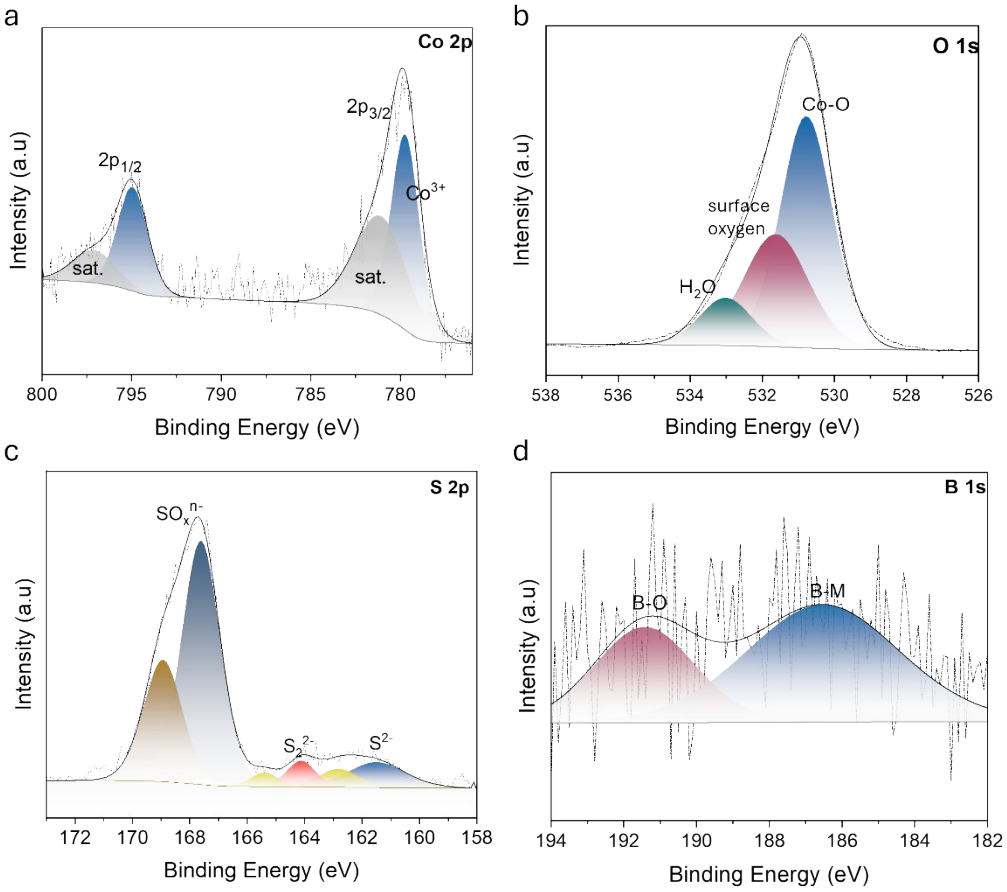

Figure S15. Deconvoluted XPS spectra of (a) Co 2p (b) O1s , (c) S2p and (d) B 1s of the post OER studies B-CoO_xS_y.

Table S3. Comparison of the OER performance of B-CoO_xS_y with representative related electrocatalysts reported in alkaline media.

Catalyst	**Electrolyte**	**η_{10} (mV)**	**Loading (mg cm^{-2})**	**Reference**
B doped CoO_xS_y	1 M KOH	189	0.700	**This work**
K-500	1 M KOH	173	0.620	10
$Co_{0.8}V_{0.2}OOH$	1 M KOH	190	0.200	11
Co-S-B nanoflakes	1 M KOH	280	0.700	12
Co_9S_8 hollow spheres	1 M KOH	285	0.100	13
Amorphous Co_xP_y	1 M KOH	287	0.205	14
CoO_xS_y@DWCNTs	1 M KOH	290	-	15
Co-P-B	1 M KOH	290	0.300	16
Co-W-B	1 M KOH	292	0.300	17
CoFeOB	1 M KOH	294	0.100	18
CoFeP NS	1 M KOH	305	-	19
Fe_3O_4@Co_9S_8/rGO nanoparticle	1 M KOH	320	0.250	20
Co-B oxide	1 M KOH	338	0.120	21
$CoWO_4$	1 M KOH	389	0.280	22
NiFeP-DBD	1 M KOH	265	0.200	23
Co_3S_4	0.1 M KOH	363	0.283	24
$Co_{1-x}S$/N-S-G	0.1 M KOH	371	0.500	25

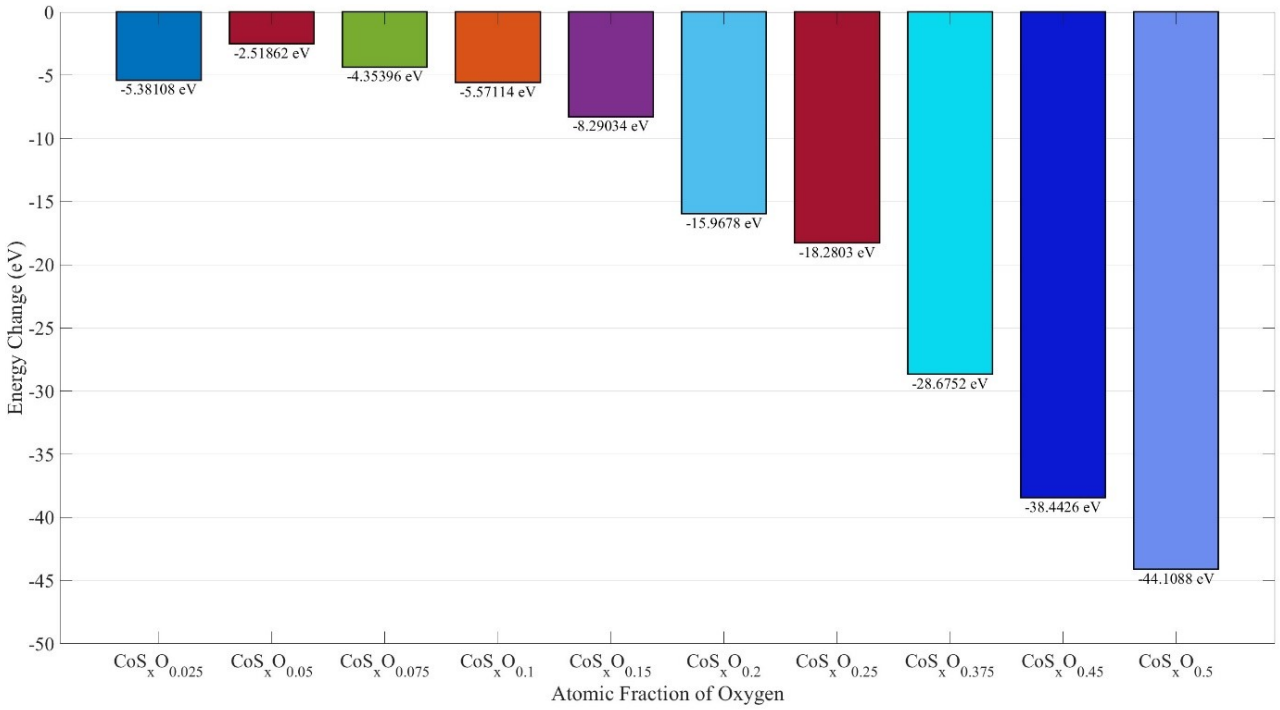

Figure S16. Bar chart of the energetic changes of doping with oxygen from the initial oxygen study

Table S4. Calculated energies and energetic changes with increasing amounts of oxygen in the system approaching the measured experimental composition.

Configuration	Total Energy (eV)
Base	-417.466
$CoS_xO_{0.025}$	-423.476
$CoS_xO_{0.05}$	-421.243
$CoS_xO_{0.75}$	-423.707
$CoS_xO_{0.1}$	-425.554
$CoS_xO_{0.15}$	-429.531
$CoS_xO_{0.2}$	-438.467
$CoS_xO_{0.25}$	-442.038
$CoS_xO_{0.38}$	-455.578
$CoS_xO_{0.45}$	-467.233
$CoS_xO_{0.5}$	-474.158

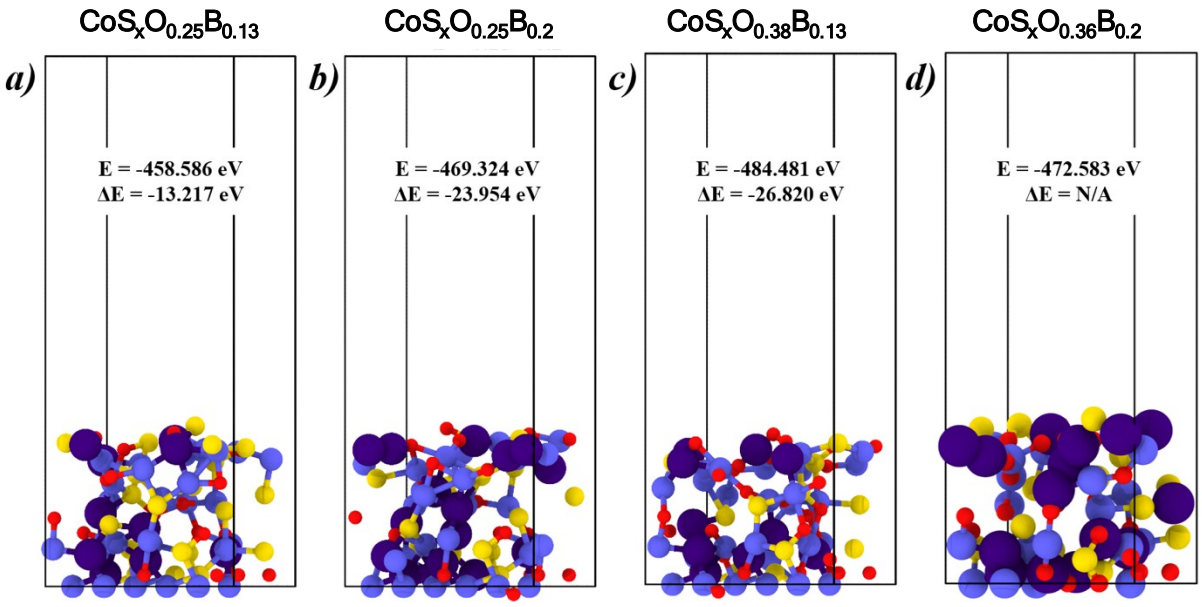

Figure S17. The relaxed models of the initial study on the effects of boron doping; red atoms represent oxygen, yellow represents sulfur, dark purple represents boron and light purple represents cobalt.

Table S5. Calculated energies and energetic changes with varying amounts of boron-doped into the system up to the measured experimental.

Configuration	Total Energy (eV)
$CoS_xO_{0.25}$	-442.038
$CoS_xO_{0.25}B_{0.13}$	-458.586
$CoS_xO_{0.25}B_{0.2}$	-469.324
$CoS_xO_{0.38}B_{0.13}$	-484.481
$CoS_xO_{0.36}B_{0.2}$	-472.583

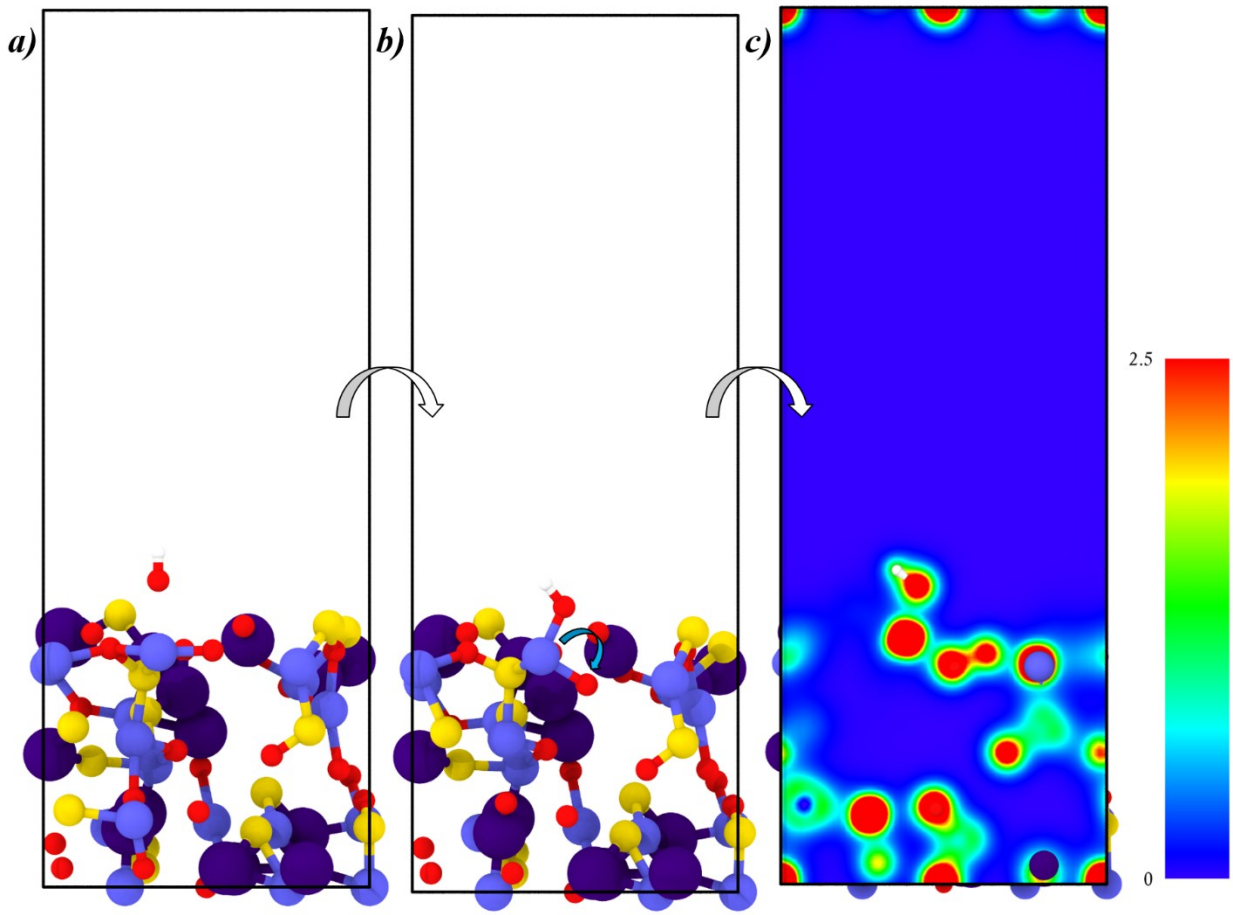

Figure S18. OH^- ion binding to cobalt on the surface of $CoS_xO_{0.36}B_{0.2}$ a) before relaxation and b) following relaxation; c) shows the charge density contour maps to aid in visualizing bonding that occurred based on electron charge distribution around the bound atoms. Oxygen atoms are colored red, sulfur atoms are colored yellow, cobalt atoms are colored light purple, and boron atoms are colored dark purple.

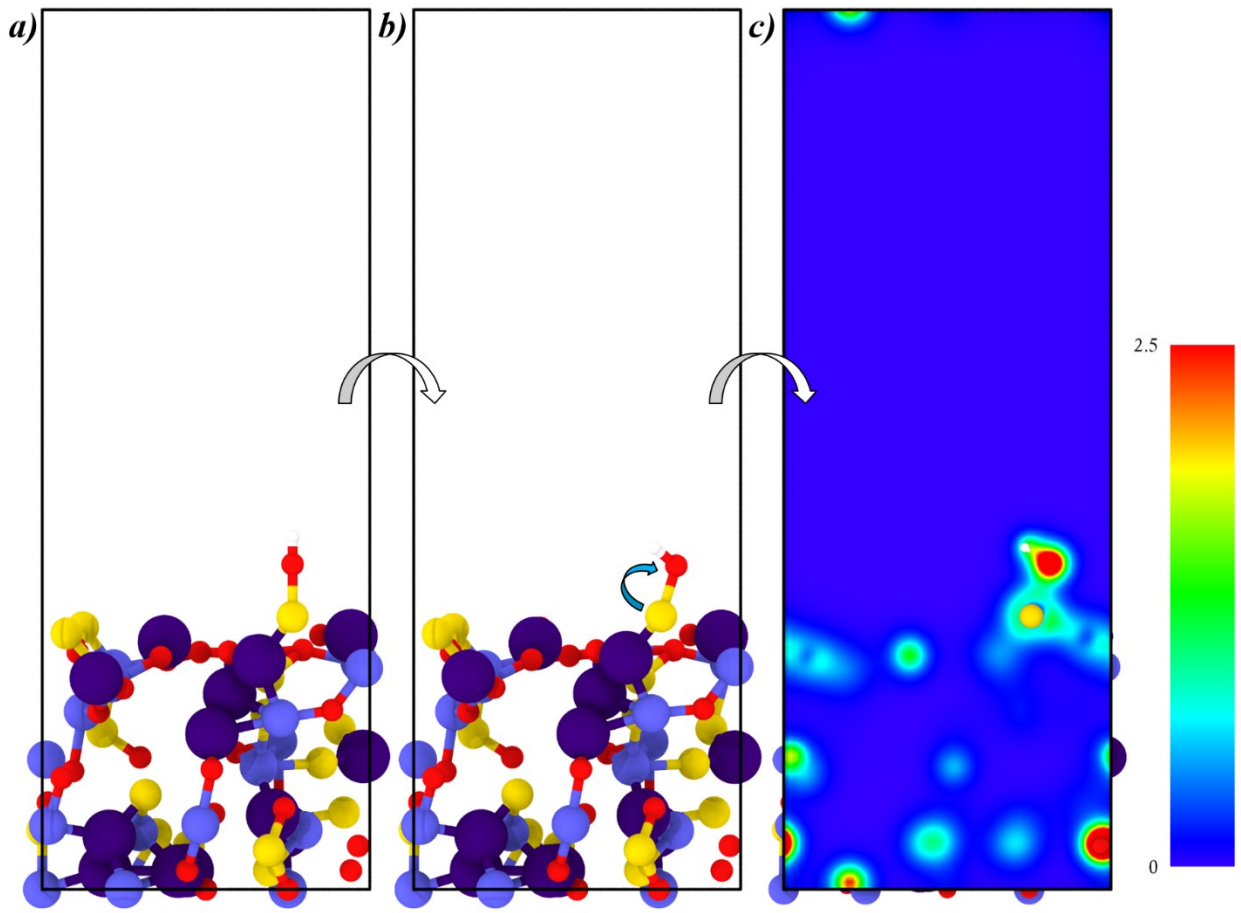

Figure S19. OH^- ion binding to sulfur on the surface of $CoS_xO_{0.36}B_{0.2}$ a) before relaxation and b) following relaxation; c) shows the charge density contour maps to aid in visualizing bonding that occurred based on electron charge distribution around the bound atoms. Oxygen atoms are colored red, sulfur atoms are colored yellow, cobalt atoms are colored light purple, and boron atoms are colored dark purple.

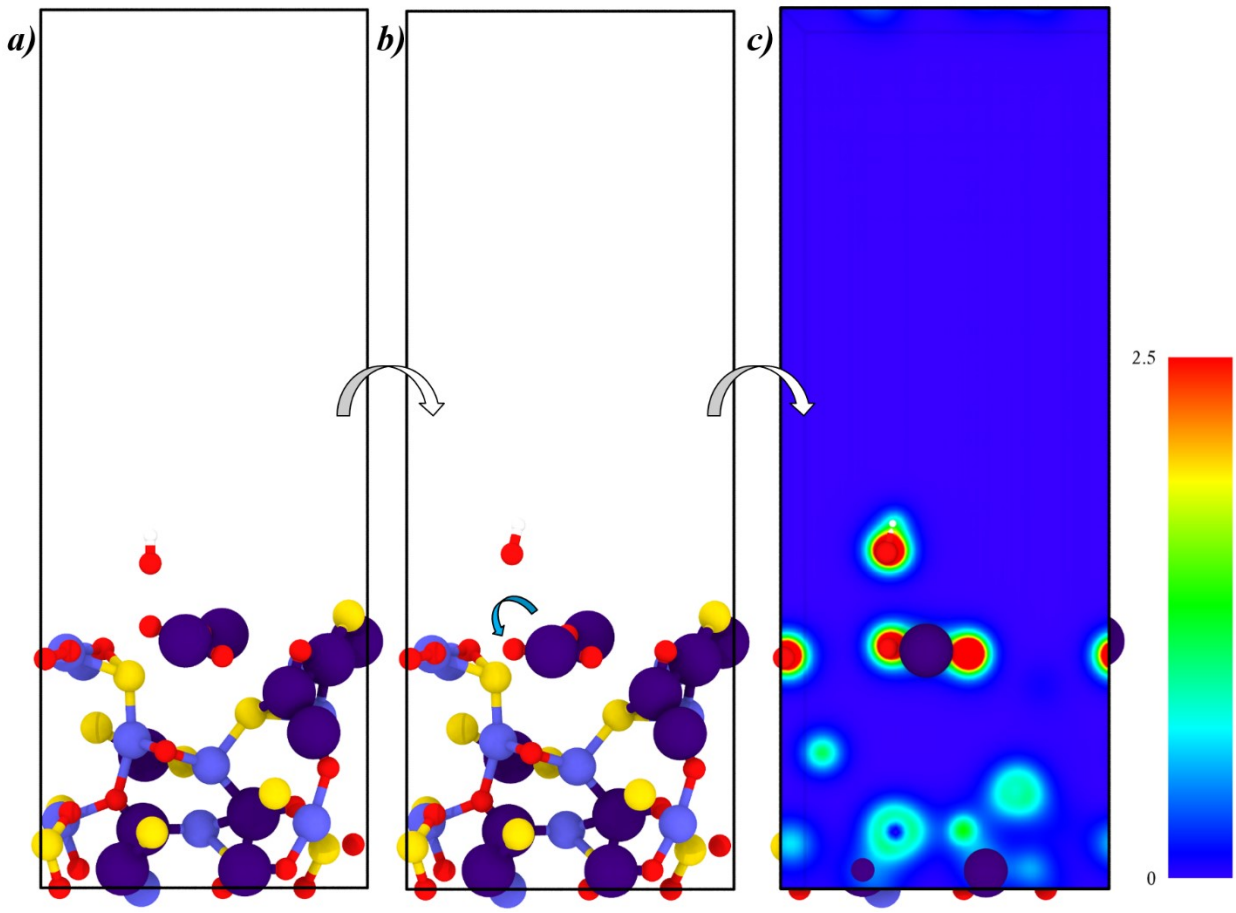

Figure S20. OH^- ion reacting with oxygen on the surface of $CoS_xO_{0.36}B_{0.2}$ a) before relaxation and b) following relaxation; c) shows the charge density contour maps to aid in visualizing bonding that occurred based on electron charge distribution around the bound atoms. Oxygen atoms are colored red, sulfur atoms are colored yellow, cobalt atoms are colored light purple, and boron atoms are colored dark purple.

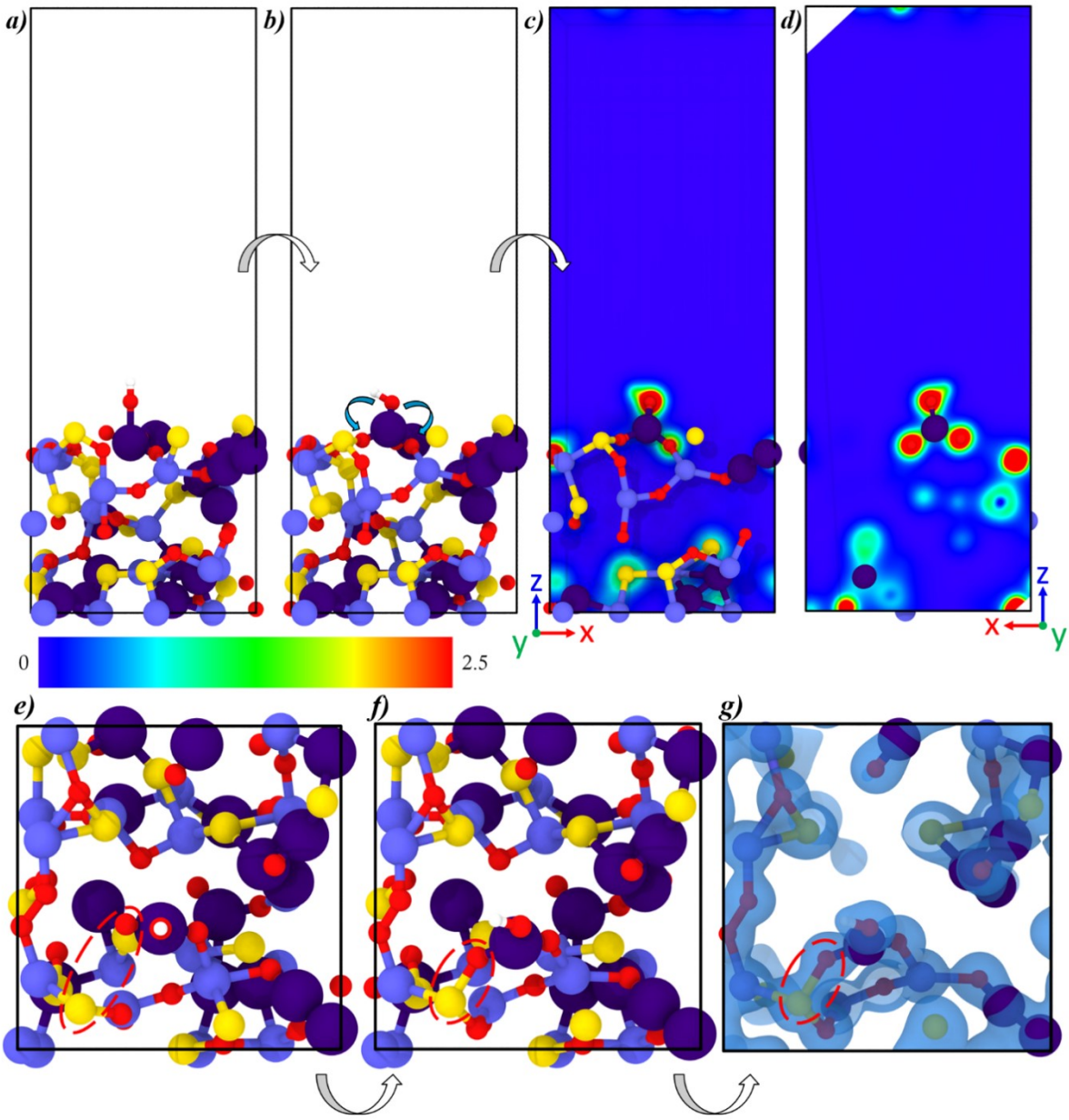

Figure S21. OH^- ion binding to boron on the surface of $CoS_xO_{0.36}B_{0.2}$ a-b) before and after relaxation; c-d) shows the charge density contour maps from two perspectives to aid in visualizing bonding that occurred. e-f) A top view of the model before and after relaxation; g) a top view of the charge density isosurface. The red dashed oval marks a newly formed S-O bond following the introduction of the OH^- ion. Oxygen atoms are colored red, sulfur atoms are colored yellow, cobalt atoms are colored light purple, and boron atoms are colored dark purple.

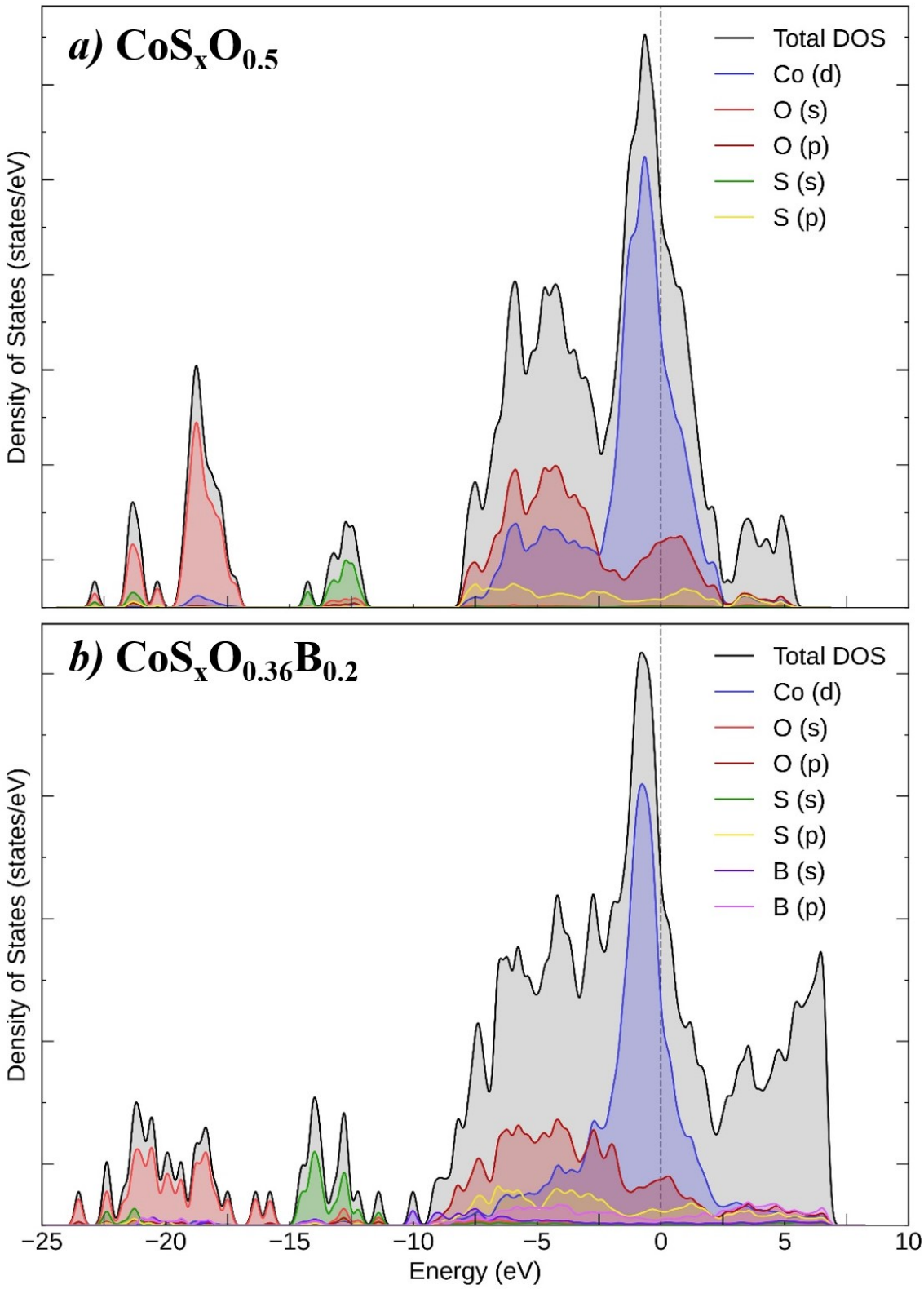

Figure S22. Combined projected DOS for a) $CoS_xO_{0.5}$ and b) $CoS_xO_{0.36}B_{0.2}$; the element types and the contributing orbital are shown in the legends for each.

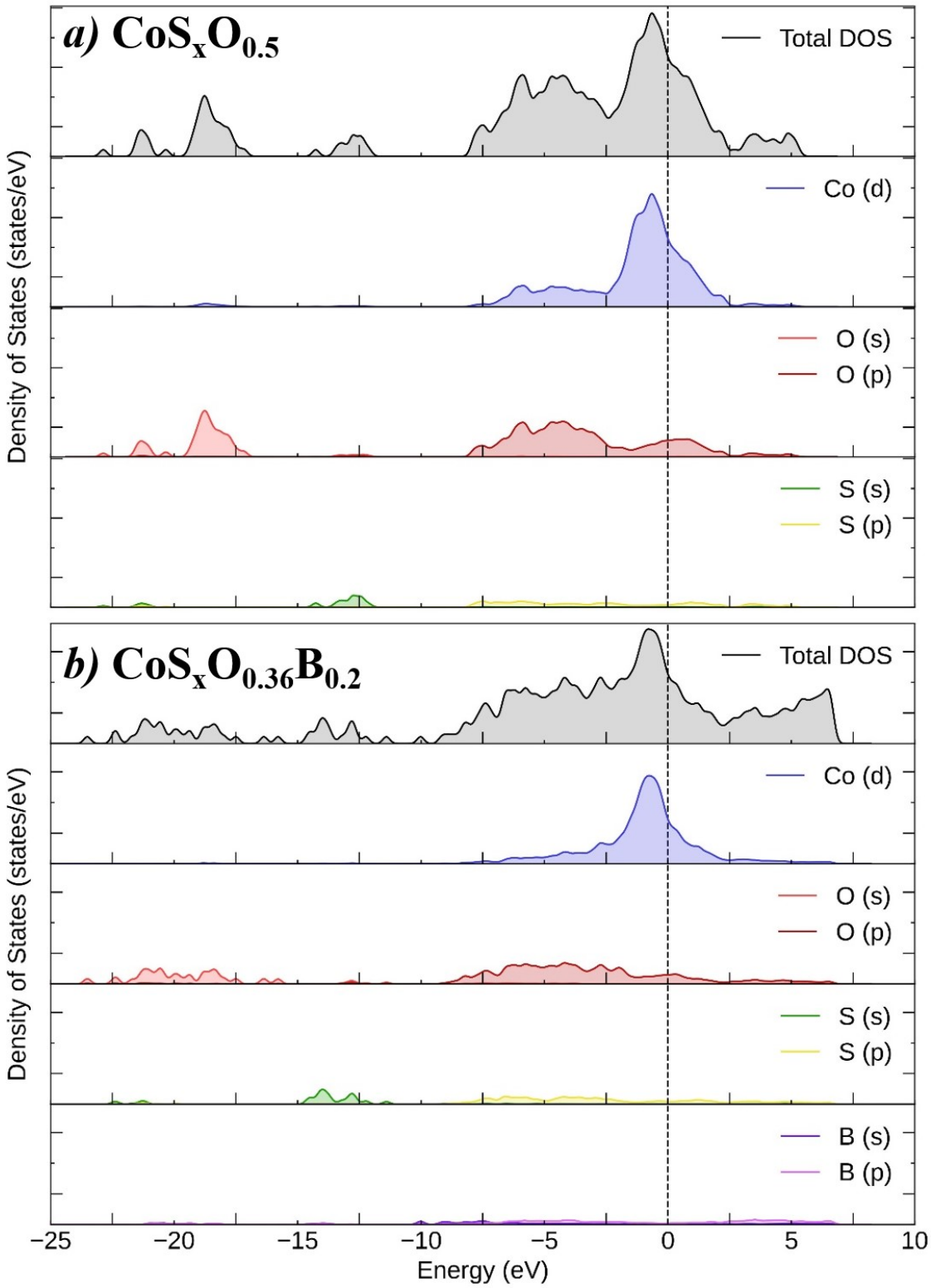

Figure S23. Projected DOS from each element for a) $CoS_xO_{0.5}$ and b) $CoS_xO_{0.36}B_{0.2}$; the element types and the contributing orbital are shown in the legends for each.

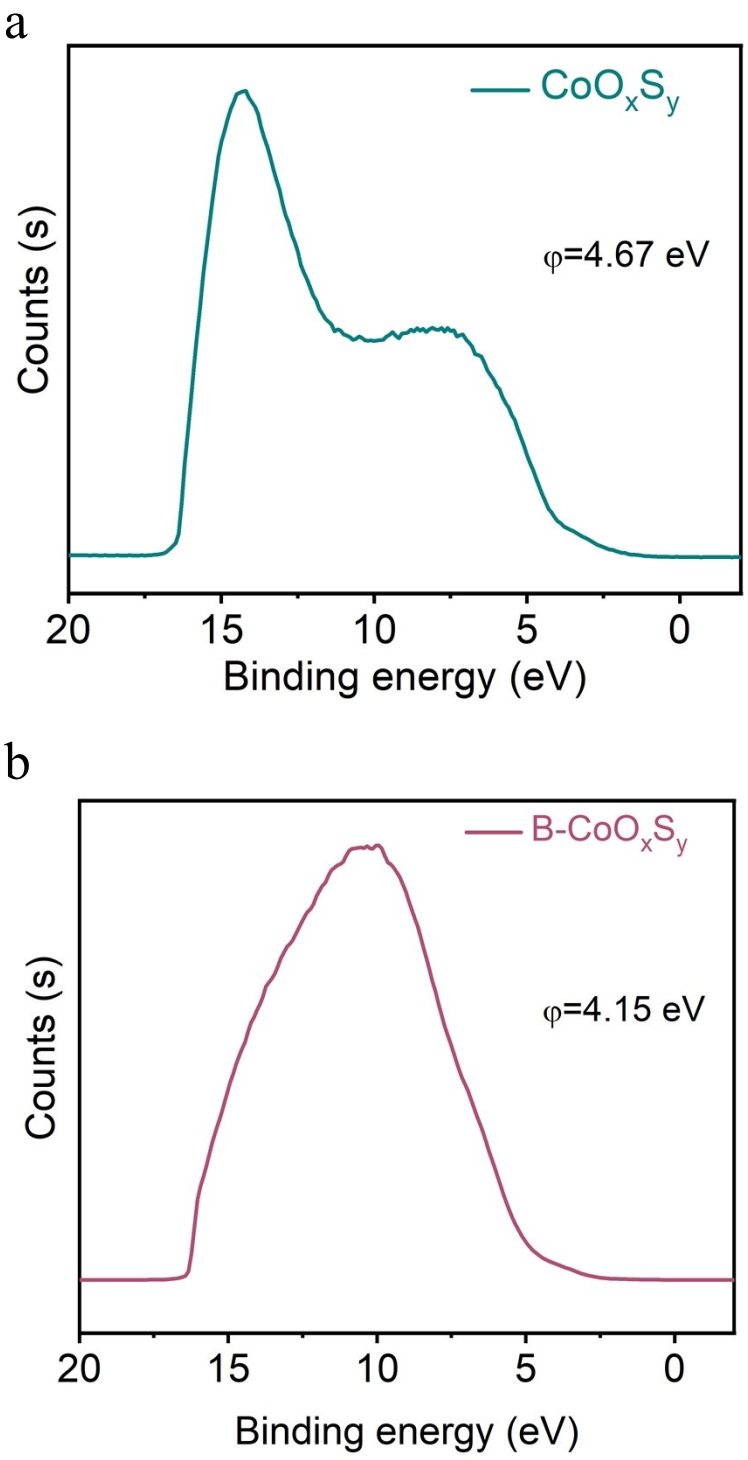

Figure S24. Ultraviolet Photoelectron Spectroscopy (UPS) measurements of CoO_xS_y and B- CoO_xS_y

References

1. S. Jung, C. C. McCrory, I. M. Ferrer, J. C. Peters and T. F. Jaramillo, Journal of Materials Chemistry A, 2016, 4, 3068-3076.
2. K. Saini, A. N. Nair, A. Yadav, L. G. Enriquez, C. J. Pollock, S. D. House, S. Yang, X. Guo and S. T. Sreenivasan, Advanced Energy Materials, 2023, 13, 2302170.
3. X. Liao, R. Lu, L. Xia, Q. Liu, H. Wang, K. Zhao, Z. Wang and Y. Zhao, Energy & Environmental Materials, 2022, 5, 157-185.
4. S. Maheshwari, Y. Li, N. Agrawal and M. J. Janik, in *Advances in Catalysis*, Elsevier, 2018, vol. 63, pp. 117-167.
5. X. Cao, Y. Hong, N. Zhang, Q. Chen, J. Masud, M. A. Zaeem and M. Nath, ACS Catalysis, 2018, 8, 8273-8289.
6. P. Cai, J. Huang, J. Chen and Z. Wen, Angewandte Chemie, 2017, 129, 4936-4939.
7. U. De Silva, J. Masud, N. Zhang, Y. Hong, W. P. Liyanage, M. A. Zaeem and M. Nath, Journal of Materials Chemistry A, 2018, 6, 7608-7622.
8. R. M. Van Ginhoven, H. Jónsson and L. R. Corrales, Physical Review B—Condensed Matter and Materials Physics, 2005, 71, 024208.
9. F. Tielens, M. Gierada, J. Handzlik and M. Calatayud, Catalysis Today, 2020, 354, 3-18.
10. N. Kumar, A. Sharma, K. Rajput, R. Kataria and S. Mehta, Heliyon, 2022, 8.
11. Y. Cui, Y. Xue, R. Zhang, J. Zhang, X. a. Li and X. Zhu, Journal of Materials Chemistry A, 2019, 7, 21911-21917.
12. A. Suryawanshi, R. A. B. John, A. Bhide, S. Gupta, M. Spreitzer, R. Patel, R. Fernandes and N. Patel, Energy & Fuels, 2024, 38, 18965-18975.
13. X. Feng, Q. Jiao, T. Liu, Q. Li, M. Yin, Y. Zhao, H. Li, C. Feng and W. Zhou, ACS Sustainable Chemistry & Engineering, 2018, 6, 1863-1871.
14. S. Anantharaj, P. N. Reddy and S. Kundu, Inorganic Chemistry, 2017, 56, 1742-1756.
15. Y. Huang, Z. Wang, S. Shen, L. Huang, W. Zhong, J. Pan and C. Li, CrystEngComm, 2022, 24, 4857-4863.
16. A. Chunduri, S. Gupta, O. Bapat, A. Bhide, R. Fernandes, M. Patel, V. Bambole, A. Miotello and N. Patel, Applied Catalysis B: Environmental, 2019, 259, 118051.
17. A. Chunduri, A. Bhide, S. Gupta, K. H. Mali, B. R. Bhagat, A. Dashora, M. Spreitzer, R. Fernandes, R. Patel and N. Patel, ACS Applied Energy Materials, 2023, 6, 4630-4641.
18. S. Gupta, M. Forster, A. Yadav, A. J. Cowan, N. Patel and M. Patel, ACS Applied Energy Materials, 2020, 3, 7619-7628.
19. H. Xu, J. Wei, C. Liu, Y. Zhang, L. Tian, C. Wang and Y. Du, Journal of colloid and interface science, 2018, 530, 146-153.
20. J. Yang, G. Zhu, Y. Liu, J. Xia, Z. Ji, X. Shen and S. Wu, Advanced Functional Materials, 2016, 26, 4712-4721.
21. M. Yu, C. Weidenthaler, Y. Wang, E. Budiyanto, E. Onur Sahin, M. Chen, S. DeBeer, O. Rüdiger and H. Tüysüz, Angewandte Chemie, 2022, 134, e202211543.
22. S. M. AlShehri, J. Ahmed, T. Ahamad, P. Arunachalam, T. Ahmad and A. Khan, RSC advances, 2017, 7, 45615-45623.
23. T. Wang, X.-Z. Fu and S. Wang, Green Energy & Environment, 2022, 7, 365-371.
24. W. Zhao, C. Zhang, F. Geng, S. Zhuo and B. Zhang, ACS nano, 2014, 8, 10909-10919.
25. X. Qiao, J. Jin, H. Fan, Y. Li and S. Liao, Journal of Materials Chemistry A, 2017, 5, 12354-12360.